



Geophysical Research Letters®



RESEARCH LETTER

10.1029/2024GL112039

Asymmetrical Ocean Carbon Responses in the Tropical Pacific Ocean to La Niña and El Niño

Chaofan Sun¹, Enhui Liao¹ , and Xueming Zhu² 

¹School of Oceanography, Shanghai Jiao Tong University, Shanghai, China, ²Southern Marine Science and Engineering Guangdong Laboratory (Zhuhai), Zhuhai, China

Key Points:

- La Niña has a broader poleward extension and longer duration than El Niño in ocean carbon responses
- The ocean carbon anomaly shifts westward during La Niña and eastward during El Niño
- These asymmetries are attributed to differing wind, precipitation, and ocean circulation anomalies

Supporting Information:

Supporting Information may be found in the online version of this article.

Correspondence to:

E. Liao,
ehliao@sjtu.edu.cn

Citation:

Sun, C., Liao, E., & Zhu, X. (2025). Asymmetrical ocean carbon responses in the tropical Pacific Ocean to La Niña and El Niño. *Geophysical Research Letters*, 52, e2024GL112039. <https://doi.org/10.1029/2024GL112039>

Received 21 AUG 2024
Accepted 5 FEB 2025

Abstract Asymmetrical ocean carbon responses to La Niña and El Niño complicate global carbon budget estimation. Using multiple ocean CO₂ data products and an advanced ocean biogeochemical model, we identified significant asymmetries in ocean carbon magnitude, spatial distribution, and duration in the tropical Pacific Ocean. La Niña enhances ocean CO₂ outgassing (0.1–0.2 PgC/yr) with a broader poleward extension (15°S–15°N) for up to 3 years, while El Niño reduces outgassing (0.2–0.4 PgC/yr) with a narrower poleward extension (10°S–10°N) for up to 1 year. The air-sea carbon flux anomaly shifts westward during La Niña and eastward during El Niño. These asymmetries are attributed to differing wind, precipitation, and ocean circulation anomalies between La Niña and El Niño. Additionally, the cumulative carbon flux remains slightly imbalanced, impacting the global ocean carbon sink balance. This study provides deeper insights into ocean carbon sink variability and highlights the need for enhanced monitoring of asymmetrical ocean carbon dynamics.

Plain Language Summary The El Niño-Southern Oscillation (ENSO) is a dominant factor in the interannual variation of global air-sea CO₂ flux. In the ocean, ENSO manifests itself as a transition between El Niño and La Niña. Because of the asymmetry between the two, it may exert a non-zero forcing, inducing imbalanced carbon responses to ENSO. In this study, we have studied the asymmetry of air-sea CO₂ flux caused by La Niña and El Niño events in the tropical Pacific Ocean. During La Niña, ocean CO₂ emissions to the atmosphere increase abnormally (0.1–0.2 PgC/yr), which lasts about 3 years with a broader poleward extension (15°S–15°N). During El Niño, ocean CO₂ emissions to the atmosphere decrease abnormally (0.2–0.4 PgC/yr), which is more intense and lasts about 1 year with a narrower poleward extension (10°S–10°N). What's more, the ocean carbon anomalies caused by La Niña tend to be more westward than those caused by El Niño. Our study shows that this is due to the combination of asymmetries in wind, rainfall, circulation anomalies, and biological processes. This study will help people understand the ocean carbon sink deeply and improve the accuracy of carbon budget estimation.

1. Introduction

Since 1850, the ocean has absorbed 26% of anthropogenic carbon (Friedlingstein et al., 2022), significantly reducing atmospheric CO₂ concentration and mitigating global warming. However, the uncertainties in estimating air-sea CO₂ flux limit an accurate understanding of the global carbon cycle and predictions of future global warming rates. The El Niño-Southern Oscillation (ENSO) is a principal driver in the global air-sea CO₂ flux interannual variability, explaining about 70% of this variability (Le Quéré et al., 2000). In the ocean, ENSO manifests itself as a shift between La Niña and El Niño (Friedlingstein et al., 2023; Timmermann et al., 2018). Although La Niña is often regarded as the mirror image of El Niño, significant differences remain in terms of amplitude, spatial structure, evolution, and global influence (Guan et al., 2019; Hoerling et al., 1997; Larkin & Harrison, 2002; Li et al., 2024). This asymmetry allows the ENSO cycle to exert a non-zero forcing on the tropical mean background state and potentially alters it (Choi et al., 2009). The asymmetrical ocean carbon responses over long time scales, with cumulative effects, may affect global carbon balance and atmospheric CO₂ concentrations. While most previous studies have concentrated on the impact of El Niño on the ocean carbon dynamics, there is a lack of systematic studies on the effect of La Niña and its distinctions from El Niño. The detailed differences in tropical Pacific Ocean carbon dynamics are delineated in this study.

Under normal conditions, the tropical Pacific Ocean is a major source of atmospheric CO₂, emitting about +0.48 PgC/yr (Ishii et al., 2014; Takahashi et al., 2009). The CO₂ outgassing occurs in the equatorial region where

© 2025. The Author(s).

This is an open access article under the terms of the [Creative Commons Attribution License](https://creativecommons.org/licenses/by/4.0/), which permits use, distribution and reproduction in any medium, provided the original work is properly cited.

upwelling transports the high dissolved inorganic carbon (DIC) from the subsurface to the surface (Feely et al., 1987, 1999, 2002; Takahashi et al., 1997; Wanninkhof et al., 1996). Other processes, such as biological activity and low-temperature effects, only partly offset the upwelling factor (Doney et al., 2009; McKinley et al., 2004; Obata & Kitamura, 2003).

El Niño weakens CO₂ outgassing while La Niña amplifies it by changing upwelling intensity, temperature, precipitation, and biological activity (Feely et al., 1987, 2002, 2006; Le Quéré et al., 2000). Extensive studies have been done on the mechanisms of the air-sea CO₂ flux anomaly caused by El Niño in the tropical Pacific Ocean based on observations and modeling results (Feely et al., 1999, 2002, 2006; Liao et al., 2020; McKinley et al., 2004; Qiao et al., 2005). The primary driving processes of CO₂ outgassing drawdown are as follows: (a) DIC replenishment from subsurface is weakened due to a weakened upwelling and a deepening thermocline, which is driven by weakened trade winds and equatorial Rossby waves during El Niño (Doney et al., 2009). (b) DIC is diluted by the eastward migration of warm-fresh pool and related increasing precipitation (Liao et al., 2020; McPhaden et al., 1998; Wang et al., 2017). (c) The air-sea CO₂ flux is reduced by weakening trade winds (Qiao et al., 2005). Additionally, the high-temperature anomaly and diminished biological consumption increase ocean surface *p*CO₂ (Behrenfeld et al., 2001; Chavez et al., 1999), but the effects of these processes are less significant compared to the others and can be canceled out.

During La Niña, almost all the processes are reversed, which drives an amplified CO₂ outgassing in the tropical Pacific Ocean (Feely et al., 2002, 2006; Ishii et al., 2009). However, these reversed processes are not completely symmetrical in terms of amplitude, distribution, and evolution between La Niña and El Niño events (Dommenget et al., 2013; Larkin & Harrison, 2002; Timmermann et al., 2018). This asymmetry probably arises from asymmetrical atmospheric response to sea surface temperature (SST) anomaly (Kang & Kug, 2002), oceanic nonlinear dynamical heating (An & Jin, 2004; Song et al., 2022), and nonlinearities in the wind-SST feedback (Karamperidou et al., 2017). The asymmetry of ENSO regarding temperature, salinity, and atmospheric circulation indicates that the La Niña anomalies are more prevalent in the western part of the equatorial Pacific Ocean with smaller amplitude, whereas El Niño anomalies tend to propagate to the eastern side of the basin with more pronounced amplitude (Chen et al., 2016; Guan et al., 2019; McPhaden & Zhang, 2009). La Niña often develops after an El Niño event and can persist for two or more years (DiNezio et al., 2017; Iwakiri & Watanabe, 2021; Wu et al., 2019), exhibiting many unique features which may induce distinct ocean carbon responses. The detailed asymmetries of ocean carbon spatial and temporal responses to ENSO and their controlling mechanisms are still not fully understood. A better understanding of these distinct ocean carbon responses to La Niña and El Niño would enhance the precision of estimating ocean carbon sink variability and the global carbon budget.

The paper is organized as follows: Section 2 describes data, model, and methods used in this study. Section 3 presents the spatial and temporal carbon responses to La Niña and El Niño, alongside the underlying physical and biological processes. In Section 4, we summarize the findings and discuss the limitations and implications of this study.

2. Data, Model, and Methods

2.1. Data and Model

The ocean *p*CO₂ and air-sea CO₂ flux data products are two reconstructed, global monthly gridded data products, derived from the Surface Ocean CO₂ Atlas (SOCAT) *p*CO₂ database (Bakker et al., 2016). The first product employs a neural network interpolation method referred to as the *p*CO₂-based SOM-FFN product (Landschützer et al., 2014). The second uses a mixed-layer scheme referred to as the *p*CO₂-based MLS product (Rödenbeck et al., 2013). The chlorophyll (Maritorena et al., 2010), nitrate (NO₃), phosphate (PO₄) (Garcia, Locarnini, et al., 2013), sea surface temperature (SST) (Banzon et al., 2016), sea surface salinity (SSS) (Melnichenko et al., 2021), mixed layer depth (MLD) (de Boyer Montégut et al., 2004), observed mooring data (TAO) (McPhaden et al., 1998; Sutton et al., 2014), and other indicators related to ocean carbon dynamics are also used in this study and detailed description refers to Text S1 in Supporting Information S1.

The model employed in this study integrates a global ocean/sea ice model with a biogeochemical module from the Geophysical Fluid Dynamics Laboratory (GFDL). The physical model comprises Modular Ocean Model version 6 (MOM6) and Sea Ice Simulator version 2 (SIS2), which are key ocean/sea-ice components of the GFDL climate and Earth System Model (CM4 and ESM4). The version of the physical model adopted here is OM4p5 with a horizontal resolution of 0.5° and eddy parameterization. The biogeochemical module is Carbon Ocean Biogeochemistry And Lower Trophic version 2 (COBALT v2), including 33 state variables such as nutrients (nitrate, phosphate, and iron), silicate, three phytoplankton groups, three zooplankton groups, three dissolved organic carbon pools, one particulate detritus pool, oxygen, and the carbonate system (Stock et al., 2020). The combined physical model and biogeochemical module are collectively referred to as MOM6-COBALT2 in this study (Adcroft et al., 2019; Stock et al., 2020).

The performance of the physical and biogeochemical model is thoroughly assessed, and it replicates well-observed physical and biogeochemical features in the tropical Pacific Ocean, including both climatological mean state and interannual variability. The assessment is illustrated in Figures S1–S9 in Supporting Information S1. For more detailed model evaluations and model configurations, including spin-up, atmospheric forcing, and initial conditions, please refer to Texts S1 and S2 in Supporting Information S1 and Liao et al. (2020).

2.2. Methods

The change in ocean $p\text{CO}_2$ ($p\text{CO}_{2w}$) is mainly related to the four elements: dissolved inorganic carbon (DIC), total alkalinity (ALK), temperature (T), and salinity (S) (Ishii et al., 2004; Le Quéré et al., 2000; Takahashi et al., 1993). This process can be expressed in Equation 1:

$$\Delta p\text{CO}_{2w} \approx \frac{\partial p\text{CO}_{2w}}{\partial \text{DIC}} \Delta \text{DIC} + \frac{\partial p\text{CO}_{2w}}{\partial \text{TALK}} \Delta \text{ALK} + \frac{\partial p\text{CO}_{2w}}{\partial T} \Delta T + \frac{\partial p\text{CO}_{2w}}{\partial S} \Delta S \quad (1)$$

Based on Equation 1, Liao et al. (2020) derived an equation to decompose the ocean $p\text{CO}_2$ temporal change into six driving processes.

$$\begin{aligned} \underbrace{\left(-\frac{\partial p\text{CO}_{2w}}{\partial \text{DIC}} \text{DIC}_{\text{FCO}_2} \right)}_{\text{Flux response}} + \underbrace{\left(\frac{\partial p\text{CO}_{2w}}{\partial t} \right)}_{p\text{CO}_2 \text{ change}} &\approx \underbrace{\left(\frac{\partial p\text{CO}_{2w}}{\partial \text{DIC}} \text{DIC}_H + \frac{\partial p\text{CO}_{2w}}{\partial \text{Alk}} \text{Alk}_H + \frac{\partial p\text{CO}_{2w}}{\partial S} S_H \right)}_{H_{\text{circ}}} \\ &+ \underbrace{\left(\frac{\partial p\text{CO}_{2w}}{\partial \text{DIC}} \text{DIC}_V + \frac{\partial p\text{CO}_{2w}}{\partial \text{Alk}} \text{Alk}_V + \frac{\partial p\text{CO}_{2w}}{\partial S} S_V \right)}_{V_{\text{circ}}} + \underbrace{\left(\frac{\partial p\text{CO}_{2w}}{\partial \text{DIC}} \text{DIC}_{\text{FW}} + \frac{\partial p\text{CO}_{2w}}{\partial \text{Alk}} \text{Alk}_{\text{FW}} + \frac{\partial p\text{CO}_{2w}}{\partial S} S_{\text{FW}} \right)}_{\text{FW}} \\ &+ \underbrace{\left(\frac{\partial p\text{CO}_{2w}}{\partial \text{DIC}} \text{DIC}_{\text{Bio}} + \frac{\partial p\text{CO}_{2w}}{\partial \text{Alk}} \text{Alk}_{\text{Bio}} \right)}_{\text{Bio}} + \underbrace{\left(\frac{\partial p\text{CO}_{2w}}{\partial T} T_H + \frac{\partial p\text{CO}_{2w}}{\partial T} T_V + \frac{\partial p\text{CO}_{2w}}{\partial T} T_Q \right)}_{\text{Thermal}} \end{aligned} \quad (2)$$

The flux response and $p\text{CO}_2$ change terms on the left-hand side (LHS) are the influence of the air-sea CO_2 flux on ocean $p\text{CO}_2$ and the ocean $p\text{CO}_2$ time tendency respectively. The five terms on the right-hand side (RHS) are the horizontal and vertical transports of dissolved species, that is, DIC, Alk, and salinity (H_{circ} and V_{circ}), the dilution/concentration effects induced by fresh-water fluxes and evaporation (FW), the biological effects due to photosynthesis, respiration, calcium carbonate dissolution/precipitation, denitrification, and nitrification (*Bio*), and vertical and horizontal transport and air-sea flux of heat (*Thermal*). On an interannual time scale, the two terms on the LHS are considered passive, representing the changes in ocean $p\text{CO}_2$ driven by the five active processes on the RHS in the tropical Pacific Ocean. For example, positive physical and biological contributions on the RHS would yield an increase in $p\text{CO}_2$ (a positive $p\text{CO}_2$ change on the LHS) and corresponding oceanic outgassing of CO_2 (positive flux response on the LHS). The detailed derivation of this equation refers to the Text S3 in Supporting Information S1.

The tropical Pacific Ocean is defined as the region spanning 15°S–15°N, 150°E to the coast of South America in this study. Due to the scarcity of observational data prior to 1990, La Niña and El Niño events are selected from 1990 to 2021, which could refer to the supporting information Section S4 (Rayner et al., 2003). To obtain interannual $p\text{CO}_2$ anomalies for both model and observations, we first remove the long-term linear trend for

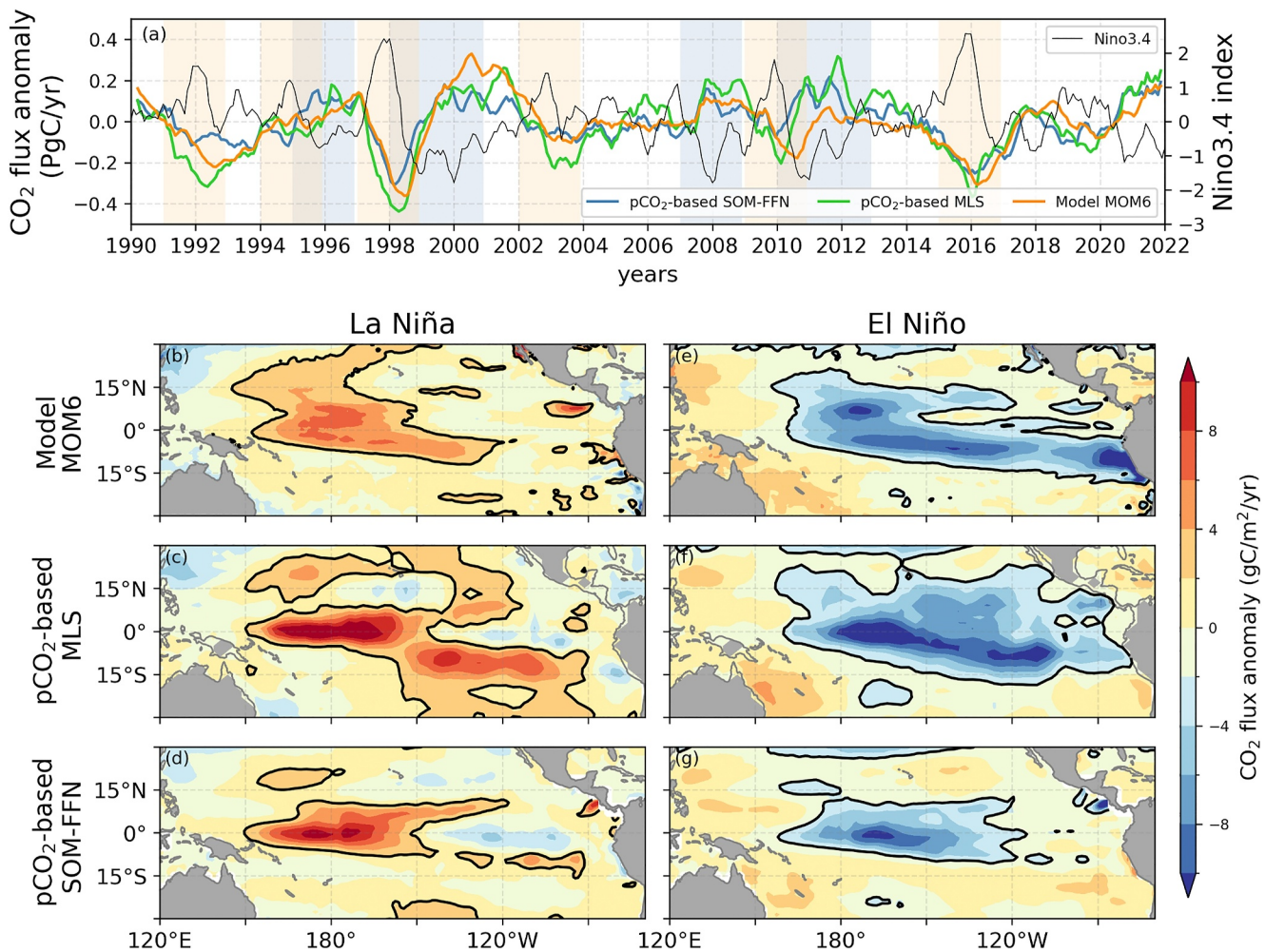


Figure 1. Time-series of (a) air-sea CO_2 flux anomaly integrated over the tropical Pacific Ocean (15°N to 15°S and 150°E to the South American coastline), and spatial distribution of air-sea CO_2 flux anomaly between La Niña (b–d) and El Niño (e–g) in two $p\text{CO}_2$ -based data products and the ocean model MOM6-COBALT2. In panel (a), the blue shading indicates La Niña events and the yellow shading indicates El Niño events. The spatial distribution is the 6-month mean (from January of year 2 to June of year 2) for a composite of six La Niña events and six El Niño events. Positive values suggest an outgassing from the ocean to the atmosphere. Observational $p\text{CO}_2$ -based products are from Rödenbeck et al. (2013) for MLS and Landschützer et al. (2014) for SOM-FFN. Black solid lines in the spatial shading map indicate isolines with a CO_2 flux anomaly of $2 \text{ gC/m}^2/\text{yr}$.

1990–2021, then subtract the climatological monthly value for the same period, and finally apply a 3-month moving average filter (Liao et al., 2020).

3. Results

3.1. Asymmetrical Air-Sea CO_2 Flux Responses to La Niña and El Niño Events

The temporal response of the CO_2 flux anomaly exhibits distinct magnitudes and durations during La Niña and El Niño events (Figure 1). A positive value indicates amplified outgassing and a negative value suggests reduced outgassing. During La Niña events, the tropical Pacific Ocean exhibits an amplified CO_2 outgassing, anomaly ranging from 0.1 to 0.2 PgC/yr , which persists for 2–3 years. Conversely, during El Niño, the ocean area shows a reduced CO_2 outgassing, with rates of 0.2–0.4 PgC/yr , and this weakened outgassing usually lasts from 6 months to 1 year. The comparison of CO_2 flux anomalies reveals a pattern of smaller magnitude and longer duration during La Niña, versus a larger magnitude and shorter duration during El Niño, which are consistent with ocean temperature, salinity, and atmospheric circulation comparisons (Burgers & Stephenson, 1999; Deser & Wallace, 1987; Ishii et al., 2004; Iwakiri & Watanabe, 2021; Wu et al., 2019). These variations in CO_2 outgassing are

closely linked to the intensity variability of equatorial upwelling among other dynamic oceanic processes in the tropical Pacific Ocean (Behrenfeld et al., 2001; Feely et al., 2006; Ishii et al., 2014). The detailed driving mechanisms responsible for these differences in magnitude and duration will be analyzed in subsequent sections.

The spatial response of air-sea CO₂ flux anomaly demonstrates distinct distribution during La Niña and El Niño events. During La Niña events, amplified CO₂ outgassing is concentrated along the equator, primarily around 180°, and extends significantly toward the poles. In contrast, during El Niño events, the reduced outgassing is positioned on the east side of 180° with a relatively modest poleward extension. Notably, the center of anomalously high CO₂ flux during La Niña events shifts westward compared to El Niño, with this shift being evident in both the equatorial region and its northern extension. The magnitude comparison indicates that the CO₂ flux anomaly is weaker during La Niña (0.042 ± 0.019 PgC/yr, 36-month average for the six events) than during El Niño (-0.062 ± 0.017 PgC/yr, 36-month average for the six events). These differences in spatial distribution and magnitude underscore distinct carbon dynamics associated with variations in circulation, precipitation, and biological activity between La Niña and El Niño. The model effectively replicates the expected differences in magnitude and spatial distribution between La Niña and El Niño as observed in data products. In addition, the two data products show inconsistent carbon responses in the eastern equatorial tropical Pacific Ocean, which may be related to sparse data availability (Landschützer et al., 2014; Rödenbeck et al., 2013).

3.2. Evolution of Asymmetrical Ocean *p*CO₂ Responses to La Niña and El Niño

Approximately 87% of the changes in air-sea carbon flux are explained by ocean *p*CO₂ variability (Figure S10 in Supporting Information S1). Additionally, changes in wind speed account for about 9% of these changes in flux, while variations in atmospheric *p*CO₂ explain roughly 2%. Thus, we focus on ocean *p*CO₂ variability to further understand the differential carbon responses to La Niña and El Niño.

Consistent with air-sea CO₂ flux variability, the ocean *p*CO₂ increases during La Niña and decreases during El Niño, which is related to the intensity of upwelling and other changed physical and biogeochemical processes during ENSO (Feely et al., 1987, 2002, 2006; Inoue & Sugimura, 1992; Jones et al., 2001; McKinley et al., 2004). The evolution of ocean *p*CO₂ anomaly every 6 months is depicted in Figure 2 to illustrate the detailed evolution of asymmetrical ocean *p*CO₂ responses to La Niña and El Niño. Year 1 is defined as the onset of La Niña and El Niño, with their peaks occurring in January and February of year 2. In line with the air-sea CO₂ flux asymmetries (Figure 1), the ocean *p*CO₂ anomaly during La Niña is characterized by a larger area, albeit with a lesser magnitude, and a longer duration compared to El Niño (Figure 2).

During the summer of La Niña year 1 (the first 6 months, Figure 2a), the ocean *p*CO₂ anomaly (8–12 μatm) initially increases in the western equatorial Pacific Ocean, centered around 165°E. Subsequently, this anomalous increase in *p*CO₂ spreads eastward across the entire equatorial Pacific Ocean, forming two distinct centers (16 μatm) along the equator, which are located in 155°E–75°E, 3°S–3°N and 150°W–110°W, 5°S–1°S. The ocean *p*CO₂ anomaly (8 μatm) extends poleward, particularly with the northern boundary reaching as far as 18°N during the spring of La Niña year 2 (January to June of year 2, Figure 2b). Notably, the northward extension is situated west of 180°, aligning with the western equatorial center. As La Niña enters the summer of year 2 (July to December of year 2, Figure 2c), the ocean *p*CO₂ anomaly diminishes from 16–20 to 12 μatm in the equatorial region, yet the affected region continues to expand both northward and southward, reaching beyond 15°S and 15°N. Both the northward and southward extensions illustrate a westward shift compared to El Niño. The pattern of rising and spreading ocean *p*CO₂ anomaly (8–16 μatm) persists in the tropical Pacific Ocean during the subsequent year (January to June of year 3, Figure 2d). After the summer of La Niña year 3, the ocean *p*CO₂ anomaly decays and reverts to normal conditions (Figure 2e).

When El Niño starts (Figure 2f), the ocean *p*CO₂ anomaly undergoes a similar evolution that the initial variability emerges in the western equatorial Pacific Ocean, and then spreads eastward, showing two centers along the equator. The western ocean *p*CO₂ anomaly center (<−12 μatm) is situated around 180°, which is further eastward compared to La Niña. During the spring of El Niño year 2 (January to June of year 2, Figure 2g), the ocean *p*CO₂ intensifies along the equator (<−16 μatm), causing the two centers to merge, making their boundary nearly indistinguishable. The subsequent poleward extension (−8 μatm) reaches only 10°N and 10°S, which is 5° less equatorward compared to La Niña. Notably, the northward extension during El Niño shifts eastward relative to La

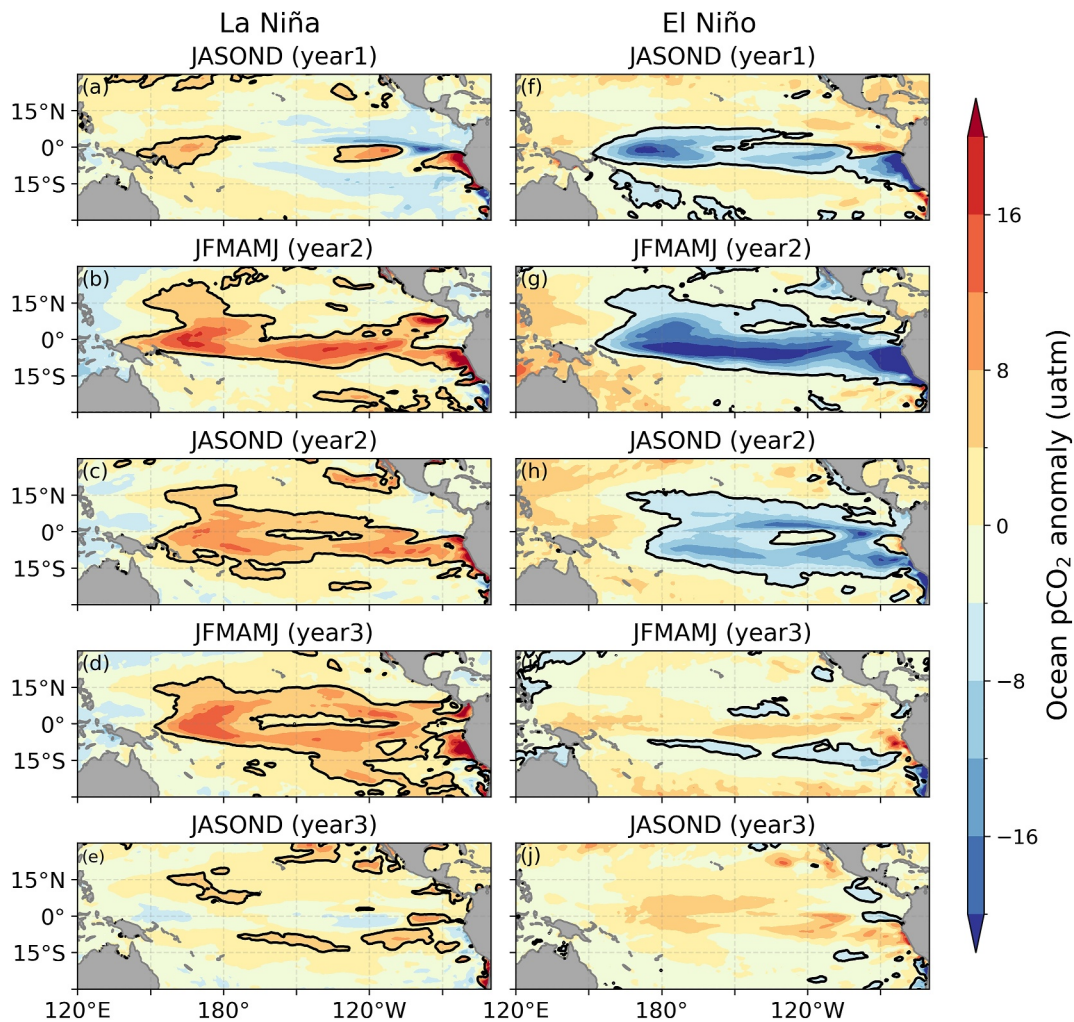


Figure 2. The evolution of ocean $p\text{CO}_2$ anomaly during La Niña (a–e) and El Niño (f–j) from July of year 1 to December of year 3 based on the MOM6-COBALT2 model result. JASOND (year 1) indicates the months from July to December in the first year, and JFMAMJ (year 2) indicates the months from January to June in the second year. ENSO peaks in January and February of year 2. The results are averaged over 6 months for a composite of six La Niña events and six El Niño events. Positive values are anomalous increases in ocean $p\text{CO}_2$. Black solid lines indicate isolines with an ocean $p\text{CO}_2$ anomaly of $4 \mu\text{atm}$.

Niña. The peak in ocean $p\text{CO}_2$ occurs only in the spring of El Niño year 2 and then decays by the following summer. During this decay period (Figure 2h), the poleward extension shows a significant eastward shift. Since El Niño is able to be separated into eastern El Niño (EP) and central El Niño (CP) (Ren & Jin, 2011; Wang et al., 2022; Yu et al., 2012), a further analysis indicates the air-sea carbon flux anomaly caused by EP El Niño is stronger, more eastward, and longer duration than CP El Niño. The intensity of the EP El Niño ($-0.11 \pm 0.038 \text{ PgC/yr}$, 36-month average for the two events) is about twice that of the CP El Niño ($-0.039 \pm 0.015 \text{ PgC/yr}$, 36-month average for the four events) and the driving mechanisms are analyzed in the Text S5 in Supporting Information S1 (Figures S14–S16 in Supporting Information S1). Overall, the evolution of ocean $p\text{CO}_2$ anomaly during El Niño exhibits intense variability ($< -16 \mu\text{atm}$) in the equatorial region, with a narrower poleward extension (10°S – 10°N) and a shorter duration (6 months–1 year) compared to La Niña.

The ocean carbon responses to La Niña and El Niño exhibit asymmetry in amplitude, spatial pattern, and duration, which shows a similar asymmetry to ocean temperature, salinity, and atmospheric circulations (Figures S7 and S11–S13 in Supporting Information S1). During La Niña, a high ocean $p\text{CO}_2$ anomaly ($> 8 \mu\text{atm}$) extends across the entire tropical Pacific Ocean, spanning from 15°S to 15°N and 140°E to 285°E , for nearly 2 years. Conversely, during El Niño, the significantly low ocean $p\text{CO}_2$ anomaly ($< -12 \mu\text{atm}$) is confined to the eastern part of the near-

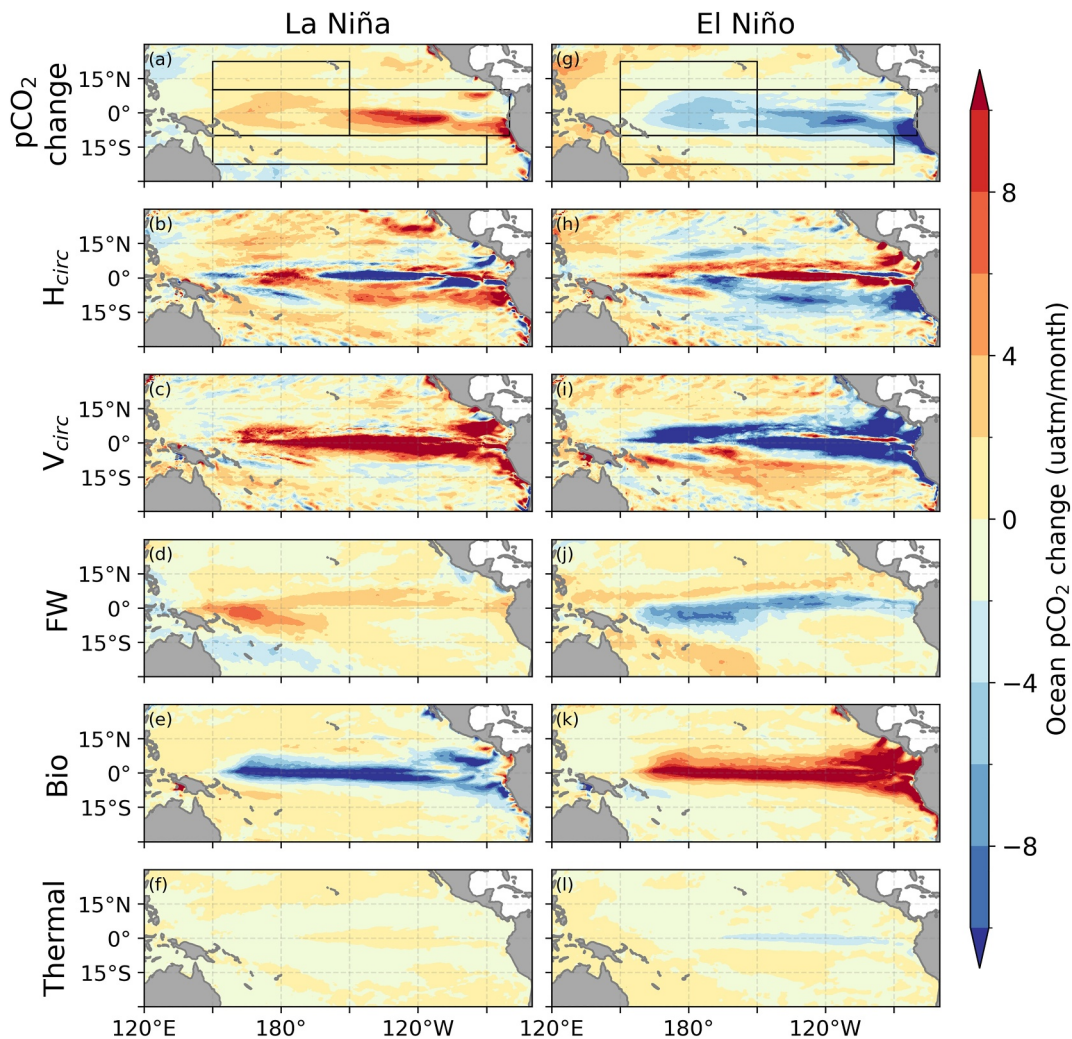


Figure 3. Processes controlling the composite carbon responses to La Niña (a–f) and El Niño (g–l) in the model between July of year 1 and June of year 2 based on Equation 2. The $p\text{CO}_2$ change (a, g), which includes $p\text{CO}_2$ time tendency and changes by the air-sea flux, can be attributed to changes in horizontal (b, h) and vertical (c, i) transports, fresh-water fluxes (d, j), biological activity (e, k), and thermal changes (f, l) ($a = b + c + d + e + f$, $g = h + i + j + k + l$, see Equation 2). Black boxes in panels (a, g) delimit the four regions for a detailed mechanisms analysis. Positive values correspond to an increase in ocean $p\text{CO}_2$.

equatorial Pacific Ocean with a weaker poleward extension (10°S–10°N), lasting only 1 year. These differences highlight the varying roles of driving forces in regulating the ocean $p\text{CO}_2$ anomaly, which will be explored in the following section.

3.3. Driving Mechanisms of Asymmetrical Ocean $p\text{CO}_2$ Response to La Niña and El Niño

We examine the mechanisms controlling the asymmetrical carbon responses observed during El Niño and La Niña. As shown in Figure 3, the two inactive terms exhibit consistent asymmetry in amplitude and distribution, resulting from the interplay of horizontal transport (circulation) and vertical transport (mixing and upwelling), fresh-water flux (dilution and concentration effect), biological activity, and thermal processes. To thoroughly examine the controlling processes behind these asymmetries, the tropical Pacific Ocean is divided into four distinct regions: (a) the western near-equatorial region, (b) the eastern near-equatorial region, (c) the northern region, and (d) the southern region (Figures 3a and 3g).

In the western near-equatorial region (Figures 3a–3f, 4a, and 4b), changes in ocean $p\text{CO}_2$ (1.8 $\mu\text{atm}/\text{month}$) during La Niña are primarily driven by vertical transport (4.3 $\mu\text{atm}/\text{month}$) and fresh-water flux term (dilution/

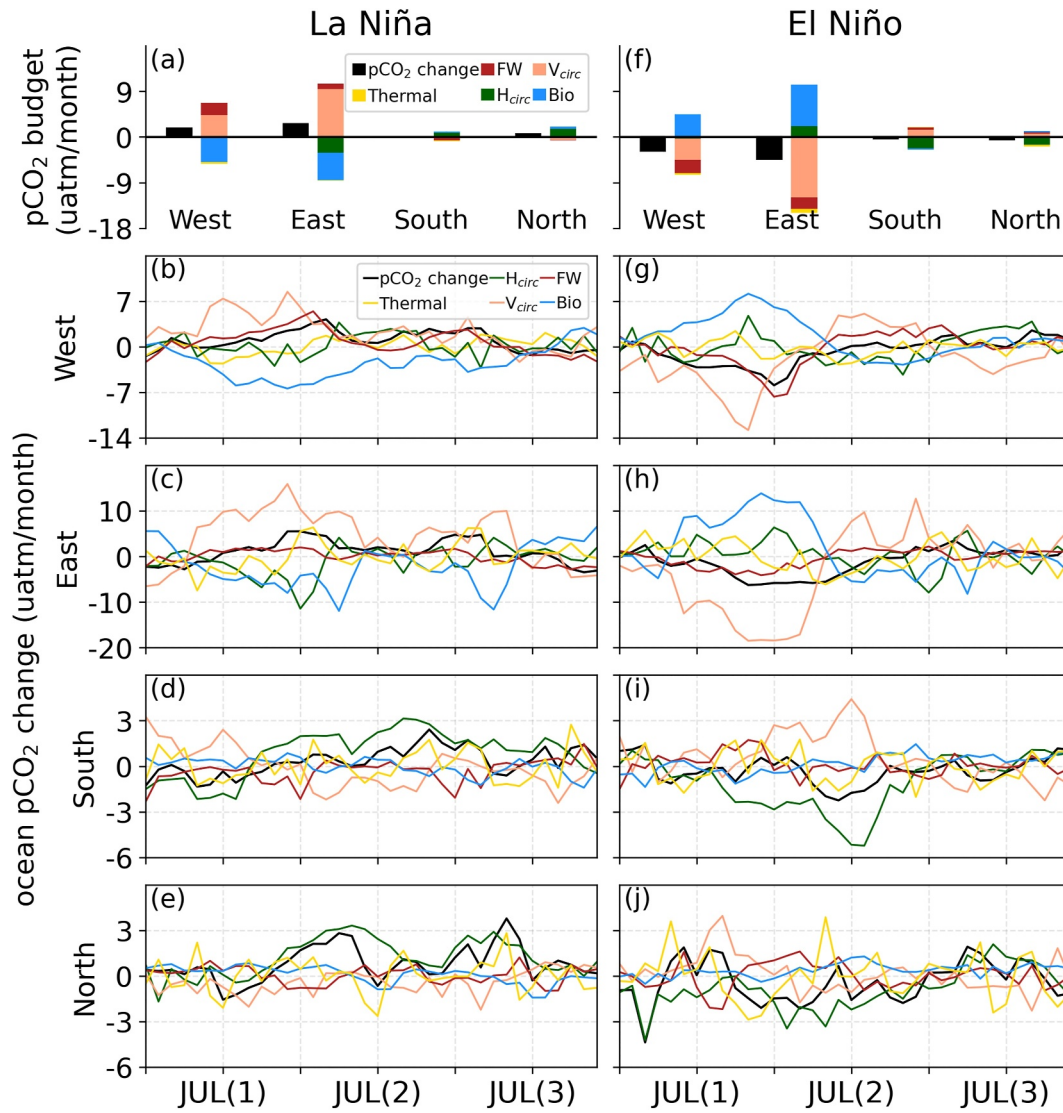


Figure 4. Ocean $p\text{CO}_2$ budget in the four regions averaged between July of year 1 and June of year 2 during La Niña (a) and El Niño (f). The time evolution of ocean $p\text{CO}_2$ budget in the four regions during La Niña (b–e) and El Niño (g–j). The regions are defined in Figures 3a and 3g. The west, east, north, and south refer to the western near-equatorial, the eastern near-equatorial, the northern, and the southern regions respectively. Positive values correspond to an increase in ocean $p\text{CO}_2$.

concentration effect, $2.4 \mu\text{atm/month}$), with biological activity ($-5.0 \mu\text{atm/month}$) partially offsetting these effects. Horizontal transport ($-0.01 \mu\text{atm/month}$) and thermal ($-0.3 \mu\text{atm/month}$) processes contribute weakly to the changes in ocean $p\text{CO}_2$ compared to other factors. Vertical transport term (Figure 3c) brings higher ocean $p\text{CO}_2$ water to the surface when La Niña drives stronger trade winds, leading to enhanced mixing and upwelling. Concurrently, as a result of stronger trade winds, precipitation anomaly moves westward to around 160°E (Figures S12b and S12d in Supporting Information S1), increasing evaporation in this area and consequently rising ocean $p\text{CO}_2$. The stronger trade winds also drive an intensified south equatorial current and enhanced poleward Ekman transport (Figure S13 in Supporting Information S1). Consequently, the zonal horizontal transport term (south equatorial current) positively contributes to high ocean $p\text{CO}_2$ by moving high ocean $p\text{CO}_2$ water along the equator from the eastern equatorial region to this area (Figure 3b). Conversely, the meridional horizontal transport term (poleward Ekman transport driven by easterly wind) reduces ocean $p\text{CO}_2$ by moving high ocean $p\text{CO}_2$ water poleward, thereby lowering the equatorial region (Figure 3b). As a result of this compensation, the net effect of horizontal transport makes a weak contribution ($-0.01 \mu\text{atm/month}$) to ocean

$p\text{CO}_2$ change in the western equatorial tropical Pacific Ocean. Underlying stronger upwelling, increased biological activity occurs in the equatorial area and consumes more carbon, leading to a negative contribution (Figures 3e and 4a).

These processes are reversed during El Niño (Figures 3g–3l and 4f–4g), with a similar contribution to the changes in ocean $p\text{CO}_2$ and carbon flux like La Niña. However, the spatial distributions of these processes shift eastward, explaining the eastward shift of ocean $p\text{CO}_2$ anomaly during El Niño. The eastward displacement of trade winds anomaly (Figures S12a and S12c in Supporting Information S1) drives intensive changes in vertical mixing and upwelling in the eastern part of the equatorial Pacific Ocean, amplifying ocean carbon response ($-2.9 \mu\text{atm/month}$) east of 180° during El Niño. In contrast, the trade winds anomaly pattern is located farther west (Figure S12 in Supporting Information S1), leading to increased ocean $p\text{CO}_2$ ($1.8 \mu\text{atm/month}$) west of 180° during La Niña. Following the east-west shift of wind anomaly, the precipitation anomaly exhibits a similar spatial distribution (Figure S12 in Supporting Information S1), which enhances the east-west displacement of ocean carbon anomaly during ENSO. Additionally, the wind and precipitation anomalies are stronger during El Niño events (Figures S12e and S12f in Supporting Information S1), which is responsible for the amplified vertical transport ($-4.1 \mu\text{atm/month}$) and fresh-water flux ($-2.7 \mu\text{atm/month}$) terms, resulting in an increased amplitude of the ocean carbon response to El Niño in this area.

In the eastern near-equatorial region (Figures 3a–3f, 4a, and 4c), the changes in $p\text{CO}_2$ ($2.8 \mu\text{atm/month}$) during La Niña are also controlled by vertical transport ($9.5 \mu\text{atm/month}$) and fresh-water flux ($1.0 \mu\text{atm/month}$), but with greater amplitude compared to the western near-equatorial region. During La Niña, stronger trade winds and reduced precipitation drive amplified vertical transport and fresh-water flux terms, leading to increased ocean $p\text{CO}_2$ (Figures 3a, 3c, and 3d). Whereas El Niño is characterized by weaker trade winds and increased precipitation, resulting in stronger vertical transport ($-11.9 \mu\text{atm/month}$) and fresh-water flux ($-2.3 \mu\text{atm/month}$) terms and then more reduction of ocean $p\text{CO}_2$ ($-4.5 \mu\text{atm/month}$, Figures 3g–3l, 4f, and 4h). The intensities of wind and precipitation anomalies during El Niño are greater than during La Niña, which is consistent with previous studies (Tang et al., 2019) and explains the asymmetrical amplitude of ocean carbon responses to ENSO. Biological activity ($-5.4 \mu\text{atm/month}$) and horizontal transport ($-3.1 \mu\text{atm/month}$) terms are the main offsetting factors. Specifically, the horizontal transport term acts to move anomalous ocean $p\text{CO}_2$ water away both zonally and meridionally, exhibiting an offsetting effect (Figures 3b and 4a). The spatial distributions of vertical transport and fresh-water flux terms follow the wind and precipitation anomalies pattern, as observed in the western near-equatorial region (Figure S12 in Supporting Information S1).

In the southern and northern regions, the variability of ocean $p\text{CO}_2$ is primarily driven by the horizontal transport term (Figure 4), which moves the anomalous ocean $p\text{CO}_2$ water (La Niña: $1.6 \mu\text{atm/month}$; El Niño: $1.5 \mu\text{atm/month}$) from the equator to these regions. Amplified horizontal transport occurs predominantly west of 180° during La Niña (Figure 3b) and east of 180° during El Niño (Figure 3h). This explains the differing distribution of poleward extension between La Niña and El Niño. In contrast to the near-equatorial region, the vertical transport term is not active, thereby offsetting the ocean $p\text{CO}_2$ anomaly driven by the horizontal transport term (Figures 4a and 4f).

The temporal evolution suggests the vertical transport term intensifies during spring and decays in summer (CP El Niño is slightly earlier), driving a cyclical pattern of ocean carbon anomaly in the western and eastern near-equatorial regions (Figures 4b, 4c, 4g, and 4h). Subsequently, the horizontal transport (poleward Ekman transport) delivers the anomalous ocean $p\text{CO}_2$ from the equatorial region to the northern and southern regions with a 3–6 months delay (Figures 4d, 4e, 4i, and 4j). This also results in a delayed cycle of ocean carbon anomaly in the northern and southern regions.

4. Discussion and Conclusion

La Niña drives amplified CO_2 outgassing, whereas El Niño induces weakened outgassing in the tropical Pacific Ocean (Figure 1). The reversed ocean carbon flux anomalies are asymmetrical in terms of amplitude, spatial distribution, and duration (Figures 1 and 2). The ocean carbon response to La Niña usually exhibits a smaller amplitude (0.1 – 0.2 PgC/yr) but affects a larger area (15°S – 15°N) and lasts longer (2–3 years). In contrast, the response to El Niño has a larger amplitude (0.2 – 0.4 PgC/yr), but impacts a smaller area (10°S – 10°N) and persists for a shorter duration (1 year). Additionally, the ocean carbon anomaly tends to shift westward during La Niña and eastward during El Niño.

The high ocean $p\text{CO}_2$ anomaly (8–12 $\mu\text{atm}/\text{month}$) initially emerges in the western equatorial Pacific Ocean, triggered by a westerly wind anomaly at the beginning of La Niña (Figure 2). Subsequently, the wind anomaly and associated Rossby wave propagate eastward along the equator, intensifying the mixing, upwelling, and thermocline tilt across the entire equatorial region. The intensified vertical transport term brings higher ocean $p\text{CO}_2$ water from the subsurface to the surface, increasing ocean $p\text{CO}_2$ (9.5 $\mu\text{atm}/\text{month}$, Figures 3c and 4). Additionally, the reduced precipitation anomaly further raises ocean $p\text{CO}_2$ through a concentration effect (2.4 $\mu\text{atm}/\text{month}$, Figures 3d and 4). Consequently, we observe a spreading of ocean $p\text{CO}_2$ anomaly along the equator, with two centers in the equatorial region (Figures 2 and 3a). The eastern center (2.8 $\mu\text{atm}/\text{month}$) displays a significantly higher ocean $p\text{CO}_2$ anomaly than does the western center (1.8 $\mu\text{atm}/\text{month}$). Under the influence of stronger easterly winds, the south equatorial current transports higher ocean $p\text{CO}_2$ water from the eastern to the western side, contributing to the western center (Figure 3b). The amplified easterly wind also drives poleward Ekman transport, which delivers anomalous ocean $p\text{CO}_2$ water from the equatorial region to the southern and northern regions (1.2 $\mu\text{atm}/\text{month}$, Figures 3b and 3c), resulting in a poleward extension of high ocean $p\text{CO}_2$ anomaly (0.4 $\mu\text{atm}/\text{month}$). These processes slightly weaken in the following summer (Figure 2c) but continue to amplify in the subsequent spring (Figure 2d). Under the continuous forcing, the anomalous ocean $p\text{CO}_2$ water almost occupies the entire tropical Pacific Ocean (15°S–15°N and 150°E–285°E) for a duration of almost 2 or 3 years (Figure 2).

El Niño drives an intense low ocean $p\text{CO}_2$ anomaly (12–16 $\mu\text{atm}/\text{month}$), exhibiting a similar evolution to La Niña in the tropical Pacific Ocean (Figures 2–4). However, compared with La Niña, the wind and precipitation anomalies during El Niño are much greater and more confined to the equatorial region (Figure S12 in Supporting Information S1). The pronounced wind and precipitation anomalies intensify ocean $p\text{CO}_2$ anomaly in the near-equatorial region, which contributes to the asymmetrical amplitude of ocean carbon responses to La Niña and El Niño. Because the easterly wind is anomalously weakened, the intensity of poleward Ekman transport during El Niño is less than that during La Niña. The weaker poleward Ekman transport only delivers anomalous ocean $p\text{CO}_2$ water as far as 10°S–10°N, which is 5° less equatorward than La Niña (Figure 2). In addition, the anomalous forcing persists only 6 months to 1 year during El Niño, which enables the expansion of anomalous ocean $p\text{CO}_2$ water to last for a shorter duration (Figures 2 and 4g–4j). These factors account for the different spatial distributions of ocean carbon anomalies between La Niña and El Niño.

As a result, the asymmetrical ocean carbon responses to La Niña and El Niño are primarily attributed to asymmetrical wind, precipitation, horizontal circulation, and biological anomalies. It should be noted that our results are largely based on surface ocean $p\text{CO}_2$ anomaly, while air-sea CO_2 flux is also affected by wind speed, atmospheric humidity, pressure, and $p\text{CO}_2$. Therefore, more detailed studies are needed to obtain the spatial and temporal characteristics of these impacts on air-sea CO_2 flux.

Moreover, our model does not fully capture the actual changes in ocean $p\text{CO}_2$ in the equatorial Pacific Ocean. For example, the slightly shallower simulation of the mixed layer depth and the biased simulation of salinity may overestimate the impact on vertical transport (Figure S3 in Supporting Information S1), which may be related to the vertical mixing scheme. This discrepancy may also lead to an underestimated $p\text{CO}_2$ variability (Liao et al., 2020). What's more, the different wind products could slightly influence the estimated contribution of ocean $p\text{CO}_2$ on the air-sea CO_2 flux interannual variability. However, these biases are very minor compared with the simulated CO_2 interannual variability which would not influence the results.

Considering both magnitude and duration, the cumulative carbon anomaly during all La Niña and El Niño events almost balances out over a long-time scale. The net carbon flux anomaly, integrated from 1990 to 2021, is about 0.71 PgC in the tropical Pacific Ocean, suggesting a slightly stronger carbon outgassing from La Niña in this period. Gruber et al. (2023) noted that there is an estimated 6 ± 5 PgC carbon loss due to climate variability or non-steady state over the past three decades (1990–2020). This imbalance between La Niña and El Niño might contribute to the observed carbon loss (about 20%). The contributions of the tropical Pacific Ocean and other ocean basins to the imbalance are estimated in the Text S6 in Supporting Information S1 (Table S1 in Supporting Information S1). The largest contribution is from the Pacific Ocean (56.2%) and the Indian Ocean (25.2%), which might be closely related to ENSO, Pacific Decadal Oscillation (PDO), and Indian Ocean Dipole (IOD) variabilities. In the context of global warming, the frequency of extreme La Niña and El Niño increases due to complex nonlinear air-sea interaction (Cai et al., 2018, 2022). We would expect a changing asymmetry of carbon variability between La Niña and El Niño. However, the detailed asymmetrical change depends on the intensity

change of La Niña and El Niño under global warming. More studies focusing on the cumulative carbon flux in the global ocean during La Niña and El Niño are essential for a better understanding of carbon loss due to climate variability.

The asymmetrical amplitude of ocean carbon flux might also influence the land-ocean carbon balance on an interannual scale. The ocean's role in offsetting land carbon flux anomaly may be diminished during La Niña and enhanced during El Niño. Under global warming, the ocean's ability to offset land carbon flux may be affected by changes in the asymmetry of ocean carbon variability. However, the detailed influence still requires further studies due to the significant uncertainty regarding the intensity changes of La Niña and El Niño under global warming. In addition, the westward shift of high ocean $p\text{CO}_2$ water could potentially amplify the ocean acidification near the Great Barrier Reef (150°E) (Mongin et al., 2016). It is crucial to closely monitor these asymmetrical carbon responses, including the variations in the ocean-land carbon balance and potential increases in ocean acidification. The carbon sink is more variable than long assumed (Gruber et al., 2023). A better understanding of ocean carbon variability during ENSO could reduce more uncertainties in the global carbon budget's interannual variability and land-ocean carbon balance, refine ocean carbon sink loss, and improve ocean acidification prediction.

Data Availability Statement

The ocean $p\text{CO}_2$ and air-sea CO_2 flux data products are derived from the Surface Ocean CO_2 Atlas (SOCAT) $p\text{CO}_2$ database (Bakker et al., 2016). The $p\text{CO}_2$ -based SOM-FFN product is from Landschützer et al. (2014), and the $p\text{CO}_2$ -based MLS product is from Rödenbeck et al. (2013). The MOM6 source code is publicly available at this site (<https://github.com/NOAA-GFDL/MOM6-examples.git>). The model results and processing codes used in this study are publicly available on Zenodo (Sun et al., 2024).

Acknowledgments

This work is supported by the project of Southern Marine Science and Engineering Guangdong Laboratory (Zhuhai) (nos. SML2023SP219), Shanghai Pujiang Program 22PJ1406300, the Ocean Negative Carbon Emissions (ONCE) Program, and Shanghai Frontiers Science Center of Polar Science (E.L.). The computations in this paper were run on the Siyuan-1 cluster supported by the Center for High Performance Computing at Shanghai Jiao Tong University. We acknowledge the National Centers for Environmental Information for providing the World Ocean Atlas data. We acknowledge the Surface Ocean CO_2 Atlas data (SOCAT; www.socat.info), which is a uniformly quality-controlled surface ocean CO_2 database. The SOCAT data is an international effort, endorsed by the International Ocean Carbon Coordination Project (IOCCP), the Surface Ocean Lower Atmosphere Study (SOLAS), and the Integrated Marine Biogeochemistry and Ecosystem Research program (IMBER).

References

- Adcroft, A., Anderson, W., Balaji, V., Blanton, C., Bushuk, M., Dufour, C. O., et al. (2019). The GFDL global ocean and sea ice model OM4.0: Model description and simulation features. *Journal of Advances in Modeling Earth Systems*, 11(10), 3167–3211. <https://doi.org/10.1029/2019MS001726>
- An, S.-I., & Jin, F.-F. (2004). Nonlinearity and asymmetry of ENSO. *Journal of Climate*, 17(12), 2399–2412. [https://doi.org/10.1175/1520-0442\(2004\)017<2399:NAAOE>2.0.CO;2](https://doi.org/10.1175/1520-0442(2004)017<2399:NAAOE>2.0.CO;2)
- Bakker, D. C. E., Pfeil, B., Landa, C. S., Metz, N., O'Brien, K. M., Olsen, A., et al. (2016). A multi-decade record of high-quality $f\text{CO}_2$ data in version 3 of the surface ocean CO_2 Atlas (SOCAT). *Earth System Science Data*, 8(2), 383–413. <https://doi.org/10.5194/essd-8-383-2016>
- Banzon, V., Smith, T. M., Chin, T. M., Liu, C., & Hankins, W. (2016). A long-term record of blended satellite and in situ sea-surface temperature for climate monitoring, modeling and environmental studies. *Earth System Science Data*, 8(1), 165–176. <https://doi.org/10.5194/essd-8-165-2016>
- Behrenfeld, M. J., Randerson, J. T., McClain, C. R., Feldman, G. C., Los, S. O., Tucker, C. J., et al. (2001). Biospheric primary production during an ENSO transition. *Science*, 291(5513), 2594–2597. <https://doi.org/10.1126/science.1055071>
- Burgers, G., & Stephenson, D. B. (1999). The “normality” of El Niño. *Geophysical Research Letters*, 26(8), 1027–1030. <https://doi.org/10.1029/1999GL900161>
- Cai, W., Ng, B., Wang, G., Santoso, A., Wu, L., & Yang, K. (2022). Increased ENSO sea surface temperature variability under four IPCC emission scenarios. *Nature Climate Change*, 12(3), 228–231. <https://doi.org/10.1038/s41558-022-01282-z>
- Cai, W., Wang, G., Dewitte, B., Wu, L., Santoso, A., Takahashi, K., et al. (2018). Increased variability of eastern Pacific El Niño under greenhouse warming. *Nature*, 564(7735), 201–206. <https://doi.org/10.1038/s41586-018-0776-9>
- Chavez, F. P., Strutton, P. G., Friederich, G. E., Feely, R. A., Feldman, G. C., Foley, D. G., & McPhaden, M. J. (1999). Biological and chemical response of the equatorial Pacific Ocean to the 1997–1998 El Niño. *Science*, 286(5447), 2126–2131. <https://doi.org/10.1126/science.286.5447.2126>
- Chen, M., Li, T., Shen, X., & Wu, B. (2016). Relative roles of dynamic and thermodynamic processes in causing evolution asymmetry between El Niño and La Niña. *Journal of Climate*, 29(6), 2201–2220. <https://doi.org/10.1175/JCLI-D-15-0547.1>
- Choi, J., An, S.-I., Dewitte, B., & Hsieh, W. W. (2009). Interactive feedback between the tropical Pacific decadal Oscillation and ENSO in a coupled general circulation model. *Journal of Climate*, 22(24), 6597–6611. <https://doi.org/10.1175/2009JCLI2782.1>
- de Boyer Montégut, C., Madec, G., Fischer, A. S., Lazar, A., & Iudicone, D. (2004). Mixed layer depth over the global ocean: An examination of profile data and a profile-based climatology. *Journal of Geophysical Research*, 109(C12), 11–12. <https://doi.org/10.1029/2004JC002378>
- Deser, C., & Wallace, J. M. (1987). El Niño events and their relation to the Southern Oscillation: 1925–1986. *Journal of Geophysical Research*, 92(C13), 14189–14196. <https://doi.org/10.1029/JC092iC13p14189>
- DiNezio, P. N., Deser, C., Okumura, Y., & Karspeck, A. (2017). Predictability of 2-year La Niña events in a coupled general circulation model. *Climate Dynamics*, 49(11), 4237–4261. <https://doi.org/10.1007/s00382-017-3575-3>
- Dommenget, D., Bayr, T., & Frauen, C. (2013). Analysis of the non-linearity in the pattern and time evolution of El Niño southern oscillation. *Climate Dynamics*, 40(11), 2825–2847. <https://doi.org/10.1007/s00382-012-1475-0>
- Doney, S. C., Lima, I., Feely, R. A., Glover, D. M., Lindsay, K., Mahowald, N., et al. (2009). Mechanisms governing interannual variability in upper-ocean inorganic carbon system and air-sea CO_2 fluxes: Physical climate and atmospheric dust. *Deep Sea Research Part II: Topical Studies in Oceanography*, 56(8), 640–655. <https://doi.org/10.1016/j.dsr2.2008.12.006>

- Feely, R. A., Boutin, J., Cosca, C. E., Dandonneau, Y., Etcheto, J., Inoue, H. Y., et al. (2002). Seasonal and interannual variability of CO₂ in the equatorial Pacific. *Deep Sea Research Part II: Topical Studies in Oceanography*, 49(13), 2443–2469. [https://doi.org/10.1016/S0967-0645\(02\)00044-9](https://doi.org/10.1016/S0967-0645(02)00044-9)
- Feely, R. A., Gammon, R. H., Taft, B. A., Pullen, P. E., Waterman, L. S., Conway, T. J., et al. (1987). Distribution of chemical tracers in the eastern equatorial Pacific during and after the 1982–1983 El Niño/Southern Oscillation event. *Journal of Geophysical Research*, 92(C6), 6545–6558. <https://doi.org/10.1029/JC092iC06p06545>
- Feely, R. A., Takahashi, T., Wanninkhof, R., McPhaden, M. J., Cosca, C. E., Sutherland, S. C., & Carr, M. (2006). Decadal variability of the air-sea CO₂ fluxes in the equatorial Pacific Ocean. *Journal of Geophysical Research*, 111(C8), C08S90. <https://doi.org/10.1029/2005JC003129>
- Feely, R. A., Wanninkhof, R., Takahashi, T., & Tans, P. (1999). Influence of El Niño on the equatorial Pacific contribution to atmospheric CO₂ accumulation. *Nature*, 398(6728), 597–601. <https://doi.org/10.1038/19273>
- Friedlingstein, P., O'Sullivan, M., Jones, M. W., Andrew, R. M., Bakker, D. C., Hauck, J., et al. (2023). Global carbon budget 2023. *Earth System Science Data*, 15(12), 5301–5369. <https://doi.org/10.5194/essd-15-5301-2023>
- Friedlingstein, P., O'Sullivan, M., Jones, M. W., Andrew, R. M., Gregor, L., Hauck, J., et al. (2022). Global carbon budget 2022. *Earth System Science Data*, 14(11), 4811–4900. <https://doi.org/10.5194/essd-14-4811-2022>
- Garcia, H. E., Locarnini, R. A., Boyer, T. P., Antonov, J. I., Baranova, O. K., Zweng, M. M., et al. (2013). *World ocean atlas 2013. Volume 4, Dissolved inorganic nutrients (phosphate, nitrate, silicate) [Atlas]*. NOAA atlas NESDIS. <https://doi.org/10.7289/V5J67DWD>
- Gruber, N., Bakker, D. C. E., DeVries, T., Gregor, L., Hauck, J., Landschützer, P., et al. (2023). Trends and variability in the ocean carbon sink. *Nature Reviews Earth & Environment*, 4(2), 119–134. <https://doi.org/10.1038/s43017-022-00381-x>
- Guan, C., Hu, S., McPhaden, M. J., Wang, F., Gao, S., & Hou, Y. (2019). Dipole structure of mixed layer salinity in response to El Niño-La Niña asymmetry in the tropical Pacific. *Geophysical Research Letters*, 46(21), 12165–12172. <https://doi.org/10.1029/2019GL084817>
- Hoerling, M. P., Kumar, A., & Zhong, M. (1997). El Niño, La Niña, and the nonlinearity of their teleconnections. *Journal of Climate*, 10(8), 1769–1786. [https://doi.org/10.1175/1520-0442\(1997\)10<1769:ENOLNA>2.0.CO;2](https://doi.org/10.1175/1520-0442(1997)10<1769:ENOLNA>2.0.CO;2)
- Inoue, H. Y., & Sugimura, Y. (1992). Variations and distributions of CO₂ in and over the equatorial Pacific during the period from the 1986/88 El Niño event to the 1988/89 La Niña event. *Tellus B: Chemical and Physical Meteorology*, 44(1), 1–22. <https://doi.org/10.3402/tellusb.v44i1.15417>
- Ishii, M., Feely, R. A., Rodgers, K. B., Park, G. H., Wanninkhof, R., Sasano, D., et al. (2014). Air–sea CO₂ flux in the Pacific Ocean for the period 1990–2009. *Biogeosciences*, 11(3), 709–734. <https://doi.org/10.5194/bg-11-709-2014>
- Ishii, M., Inoue, H. Y., Midorikawa, T., Saito, S., Tokieda, T., Sasano, D., et al. (2009). Spatial variability and decadal trend of the oceanic CO₂ in the western equatorial Pacific warm/fresh water. *Deep Sea Research Part II: Topical Studies in Oceanography*, 56(8), 591–606. <https://doi.org/10.1016/j.dsr2.2009.01.002>
- Ishii, M., Saito, S., Tokieda, T., Kawano, T., Matsumoto, K., & Yoshikawa-Inoue, H. (2004). Variability of surface layer CO₂ parameters in the western and central equatorial Pacific. *Global Environmental Change in the Ocean and on Land*, 59–94. <https://www.researchgate.net/publication/228496941>
- Iwakiri, T., & Watanabe, M. (2021). Mechanisms linking multi-year La Niña with preceding strong El Niño. *Scientific Reports*, 11(1), 17465. <https://doi.org/10.1038/s41598-021-96056-6>
- Jones, C. D., Collins, M., Cox, P. M., & Spall, S. A. (2001). The carbon cycle response to ENSO: A coupled climate–carbon cycle model study. *Journal of Climate*, 14(21), 4113–4129. [https://doi.org/10.1175/1520-0442\(2001\)014<4113:TCCRTE>2.0.CO;2](https://doi.org/10.1175/1520-0442(2001)014<4113:TCCRTE>2.0.CO;2)
- Kang, I.-S., & Kug, J.-S. (2002). El Niño and La Niña sea surface temperature anomalies: Asymmetry characteristics associated with their wind stress anomalies. *Journal of Geophysical Research*, 107(D19), ACL1-1–ACL1-10. <https://doi.org/10.1029/2001JD000393>
- Karamperidou, C., Jin, F.-F., & Conroy, J. L. (2017). The importance of ENSO nonlinearities in tropical Pacific response to external forcing. *Climate Dynamics*, 49(7), 2695–2704. <https://doi.org/10.1007/s00382-016-3475-y>
- Landschützer, P., Gruber, N., Bakker, D. C. E., & Schuster, U. (2014). Recent variability of the global ocean carbon sink. *Global Biogeochemical Cycles*, 28(9), 927–949. <https://doi.org/10.1002/2014GB004853>
- Larkin, N. K., & Harrison, D. E. (2002). ENSO warm (El Niño) and cold (La Niña) event life cycles: Ocean surface anomaly patterns, their symmetries, asymmetries, and implications. *Journal of Climate*, 15(10), 1118–1140. [https://doi.org/10.1175/1520-0442\(2002\)015<1118:EWENOA>2.0.CO;2](https://doi.org/10.1175/1520-0442(2002)015<1118:EWENOA>2.0.CO;2)
- Le Quéré, C., Orr, J. C., Monfray, P., Aumont, O., & Madec, G. (2000). Interannual variability of the oceanic sink of CO₂ from 1979 through 1997. *Global Biogeochemical Cycles*, 14(4), 1247–1265. <https://doi.org/10.1029/1999GB900049>
- Li, X., Yu, J.-Y., & Ding, R. (2024). El Niño-La Niña asymmetries in the changes of ENSO complexities and dynamics since 1990. *Geophysical Research Letters*, 51(6), e2023GL106395. <https://doi.org/10.1029/2023GL106395>
- Liao, E., Resplandy, L., Liu, J., & Bowman, K. W. (2020). Amplification of the ocean carbon sink during El Niños: Role of poleward Ekman transport and influence on atmospheric CO₂. *Global Biogeochemical Cycles*, 34(9), e2020GB006574. <https://doi.org/10.1029/2020GB006574>
- Maritorena, S., d'Andon, O. H. F., Mangin, A., & Siegel, D. A. (2010). Merged satellite ocean color data products using a bio-optical model: Characteristics, benefits and issues. *Remote Sensing of Environment*, 114(8), 1791–1804. <https://doi.org/10.1016/j.rse.2010.04.002>
- McKinley, G. A., Follows, M. J., & Marshall, J. (2004). Mechanisms of air-sea CO₂ flux variability in the equatorial Pacific and the North Atlantic. *Global Biogeochemical Cycles*, 18(2), 1–14. <https://doi.org/10.1029/2003GB002179>
- McPhaden, M. J., Busalacchi, A. J., Cheney, R., Donguy, J.-R., Gage, K. S., Halpern, D., et al. (1998). The tropical ocean–global atmosphere observing system: A decade of progress. *Journal of Geophysical Research*, 103(C7), 14169–14240. <https://doi.org/10.1029/97JC02906>
- McPhaden, M. J., & Zhang, X. (2009). Asymmetry in zonal phase propagation of ENSO sea surface temperature anomalies. *Geophysical Research Letters*, 36(13), 245–257. <https://doi.org/10.1029/2009GL038774>
- Melnichenko, O., Hacker, P., Potemra, J., Meissner, T., & Wentz, F. (2021). Aquarius/SMAP sea surface salinity optimum interpolation analysis. IPRC Technical Note No. 7. Retrieved from https://iprc.soest.hawaii.edu/aquarius/oleg/oisss/GLB/OISSS_Product_Notes.pdf
- Mongin, M., Baird, M. E., Tilbrook, B., Matear, R. J., Lenton, A., Herzfeld, M., et al. (2016). The exposure of the Great Barrier Reef to ocean acidification. *Nature Communications*, 7(1), 10732. <https://doi.org/10.1038/ncomms10732>
- Obata, A., & Kitamura, Y. (2003). Interannual variability of the sea-air exchange of CO₂ from 1961 to 1998 simulated with a global ocean circulation–biogeochemistry model. *Journal of Geophysical Research*, 108(C11), 3337. <https://doi.org/10.1029/2001JC001088>
- Qiao, R., Wang, Z., Chen, S., Li, S., Yu, Y., & lv, H. (2005). Distribution of marine carbon dioxide and its relationship with other marine parameters and air-sea anomalies. *Acta Oceanologica Sinica*, 27(6), 30–37. https://www.alljournals.cn/view_abstract.aspx?pcid=E62459D214FD64A3C8082E4EDIABABED5711027BBBDD35B&cid=2D9C75573FA3E416&jid=C138594556EC32C55DD11D85CC36D0F4&aid=16D5EEFB006C6B19&yid=2DD7160C83D0ACED&vid=&iid=&sid=&eid=&id=from_abstract=1

- Rayner, N. A., Parker, D. E., Horton, E. B., Folland, C. K., Alexander, L. V., Rowell, D. P., et al. (2003). Global analyses of sea surface temperature, sea ice, and night marine air temperature since the late nineteenth century. *Journal of Geophysical Research*, *108*(D14), 4407. <https://doi.org/10.1029/2002JD002670>
- Ren, H.-L., & Jin, F.-F. (2011). Niño indices for two types of ENSO. *Geophysical Research Letters*, *38*(4). <https://doi.org/10.1029/2010GL046031>
- Rödenbeck, C., Keeling, R. F., Bakker, D. C. E., Metzl, N., Olsen, A., Sabine, C., & Heimann, M. (2013). Global surface-ocean pCO₂ and sea-air CO₂ flux variability from an observation-driven ocean mixed-layer scheme. *Ocean Science*, *9*(2), 193–216. <https://doi.org/10.5194/os-9-193-2013>
- Song, X., Zhang, R., & Rong, X. (2022). Dynamic causes of ENSO decay and its asymmetry. *Journal of Climate*, *35*(2), 445–462. <https://doi.org/10.1175/JCLI-D-21-0138.1>
- Stock, C. A., Dunne, J. P., Fan, S., Ginoux, P., John, J., Krasting, J. P., et al. (2020). Ocean biogeochemistry in GFDL's Earth system model 4.1 and its response to increasing atmospheric CO₂. *Journal of Advances in Modeling Earth Systems*, *12*(10), e2019MS002043. <https://doi.org/10.1029/2019MS002043>
- Sun, C., Liao, E., & Zhu, X. (2024). MOM6-COBALT2 model results for asymmetrical ocean carbon responses to La Nina and El Nino in the tropical Pacific Ocean [Dataset]. *Zenodo*. <https://doi.org/10.5281/zenodo.13329219>
- Sutton, A. J., Sabine, C. L., Maenner-Jones, S., Lawrence-Slavas, N., Meinig, C., Feely, R. A., et al. (2014). A high-frequency atmospheric and seawater pCO₂ data set from 14 open-ocean sites using a moored autonomous system. *Earth System Science Data*, *6*(2), 353–366. <https://doi.org/10.5194/essd-6-353-2014>
- Takahashi, T., Feely, R. A., Weiss, R. F., Wanninkhof, R. H., Chipman, D. W., Sutherland, S. C., et al. (1997). Global air-sea flux of CO₂: An estimate based on measurements of sea-air pCO₂ difference. *Proceedings of the National Academy of Sciences of the United States of America*, *94*(16), 8292–8299. <https://doi.org/10.1073/pnas.94.16.8292>
- Takahashi, T., Olafsson, J., Goddard, J. G., Chipman, D. W., & Sutherland, S. C. (1993). Seasonal variation of CO₂ and nutrients in the high-latitude surface oceans: A comparative study. *Global Biogeochemical Cycles*, *7*(4), 843–878. <https://doi.org/10.1029/93GB02263>
- Takahashi, T., Sutherland, S. C., Wanninkhof, R., Sweeney, C., Feely, R. A., Chipman, D. W., et al. (2009). Climatological mean and decadal change in surface ocean pCO₂, and net sea-air CO₂ flux over the global oceans. *Deep Sea Research Part II: Topical Studies in Oceanography*, *56*(8), 554–577. <https://doi.org/10.1016/j.dsr2.2008.12.009>
- Tang, Y., Li, L., Wang, B., Lin, P., Dong, W., & Xia, K. (2019). The collective contribution of atmospheric and oceanic components to ENSO asymmetry. *Atmosphere*, *10*(8), 469. <https://doi.org/10.3390/atmos10080469>
- Timmermann, A., An, S.-I., Kug, J.-S., Jin, F.-F., Cai, W., Capotondi, A., et al. (2018). El Niño–Southern Oscillation complexity. *Nature*, *559*(7715), 535–545. <https://doi.org/10.1038/s41586-018-0252-6>
- Wang, C., Deser, C., Yu, J.-Y., DiNezio, P., & Clement, A. (2017). El Niño and Southern Oscillation (ENSO): A review. In P. W. Glynn, D. P. Manziello, & I. C. Enochs (Eds.), *Coral reefs of the eastern tropical Pacific: Persistence and loss in a dynamic environment* (Vol. 8, pp. 85–106). Springer. https://doi.org/10.1007/978-94-017-7499-4_4
- Wang, C., Li, J., Liu, Q., Huete, A., Li, L., Dong, Y., & Zhao, J. (2022). Eastern-Pacific and Central-Pacific types of ENSO elicit diverse responses of vegetation in the West Pacific Region. *Geophysical Research Letters*, *49*(3), e2021GL096666. <https://doi.org/10.1029/2021GL096666>
- Wanninkhof, R., Feely, R. A., Chen, H., Cosca, C., & Murphy, P. P. (1996). Surface water fCO₂ in the eastern equatorial Pacific during the 1992–1993 El Niño. *Journal of Geophysical Research*, *101*(C7), 16333–16343. <https://doi.org/10.1029/96JC01348>
- Wu, X., Okumura, Y. M., & DiNezio, P. N. (2019). What controls the duration of El Niño and La Niña events? *Journal of Climate*, *32*(18), 5941–5965. <https://doi.org/10.1175/JCLI-D-18-0681.1>
- Yu, J.-Y., Zou, Y., Kim, S. T., & Lee, T. (2012). The changing impact of El Niño on US winter temperatures. *Geophysical Research Letters*, *39*(15), L15702. <https://doi.org/10.1029/2012GL052483>

References From the Supporting Information

- Garcia, H. E., Boyer, T. P., Locarnini, R. A., Antonov, J. I., Mishonov, A. V., Baranova, O. K., et al. (2013). *World ocean atlas 2013. Volume 3. Dissolved oxygen, apparent oxygen utilization, and oxygen saturation [Atlas]* (Vol. 3). NOAA atlas NESDIS. <https://doi.org/10.7289/V5XG9P2W>
- Khatiwal, S., Tanhua, T., Mikaloff Fletcher, S., Gerber, M., Doney, S. C., Graven, H. D., et al. (2013). Global ocean storage of anthropogenic carbon. *Biogeosciences*, *10*(4), 2169–2191. <https://doi.org/10.5194/bg-10-2169-2013>
- Liao, E., Lu, W., Xue, L., & Du, Y. (2024). Weakening Indian Ocean carbon uptake in 2015: The role of amplified basin-wide warming and reduced Indonesian throughflow. *Limnology and Oceanography Letters*, *9*(4), 442–451. <https://doi.org/10.1002/lol2.10397>
- Locarnini, R. A., Mishonov, A. V., Antonov, J. I., Boyer, T. P., Garcia, H. E., Baranova, O. K., et al. (2013). *World ocean atlas 2013. In Temperature [Atlas]* (Vol. 1). NOAA atlas NESDIS. <https://doi.org/10.7289/V55X26VD>
- Lovenduski, N. S., Gruber, N., Doney, S. C., & Lima, I. D. (2007). Enhanced CO₂ outgassing in the Southern Ocean from a positive phase of the southern annular mode. *Global Biogeochemical Cycles*, *21*(2), GB2026. <https://doi.org/10.1029/2006GB002900>
- Olsen, A., Key, R. M., van Heuven, S., Lauvset, S. K., Velo, A., Lin, X., et al. (2016). The Global Ocean Data Analysis Project version 2 (GLODAPv2)—An internally consistent data product for the World Ocean. *Earth System Science Data*, *8*(2), 297–323. <https://doi.org/10.5194/essd-8-297-2016>
- Sarmiento, J., Gruber, N., & McElroy, M. (2007). Ocean biogeochemical dynamics. *Physics Today*, *60*(6), 65. <https://doi.org/10.1063/1.2754608>
- Stock, C. A., Dunne, J. P., & John, J. G. (2014). Global-scale carbon and energy flows through the marine planktonic food web: An analysis with a coupled physical–biological model. *Progress in Oceanography*, *120*, 1–28. <https://doi.org/10.1016/j.pocan.2013.07.001>
- Takahashi, T., Sutherland, S. C., Feely, R. A., & Cosca, C. E. (2003). Decadal variation of the surface water pCO₂ in the western and central equatorial Pacific. *Science*, *302*(5646), 852–856. <https://doi.org/10.1126/science.1088570>
- Wanninkhof, R. (2014). Relationship between wind speed and gas exchange over the ocean revisited. *Limnology and Oceanography: Methods*, *12*(6), 351–362. <https://doi.org/10.4319/lom.2014.12.351>
- Weiss, R. F., & Price, B. A. (1980). Nitrous oxide solubility in water and seawater. *Marine Chemistry*, *8*(4), 347–359. [https://doi.org/10.1016/0304-4203\(80\)90024-9](https://doi.org/10.1016/0304-4203(80)90024-9)
- Zweng, M. M., Reagan, J. R., Antonov, J. I., Locarnini, R. A., Mishonov, A. V., Boyer, T. P., et al. (2013). *World ocean atlas 2013. In Salinity [Atlas]* (Vol. 2). NOAA atlas NESDIS. <https://doi.org/10.7289/V5251G4D>